

Computational study of the role of gas-phase oxidation in CW laser ablation of Al target in an external supersonic air flow

Alexey N. Volkov · Leonid V. Zhigilei

Received: 30 July 2012 / Accepted: 3 August 2012 / Published online: 12 October 2012
© Springer-Verlag Berlin Heidelberg 2012

Abstract Vapor expansion from Al target irradiated by a continuous wave laser into a supersonic external air flow is investigated in kinetic simulations performed for values of pressure in the external flow ranging from 50 Pa to 10000 Pa. The direct simulation Monte Carlo method enhanced with a simplified description of Al vapor burning in air is used in the simulations. The results of the simulations reveal a significant effect of the external gas pressure on the flow structures and the mechanisms of the alumina and oxygen transport to the target surface. At small values of pressure, the transport of both alumina and oxygen is controlled by diffusion and the formation of alumina film on the surface of the laser spot is dominated by the direct sedimentation of alumina from the gas flow. In this regime, the flux of oxygen to the laser spot is by an order of magnitude smaller than that of alumina. At higher values of pressure, the diffusion cannot directly deliver oxygen and alumina to the surface of the laser spot, but the circulating flow generated upstream the spot can effectively trap alumina formed in the flame zone and deposit it to the target surface. In this regime, the likely mechanism of the alumina film formation within the spot is the heterogeneous oxidation and growth of the film from the upstream edge of the spot in the downstream direction.

1 Introduction

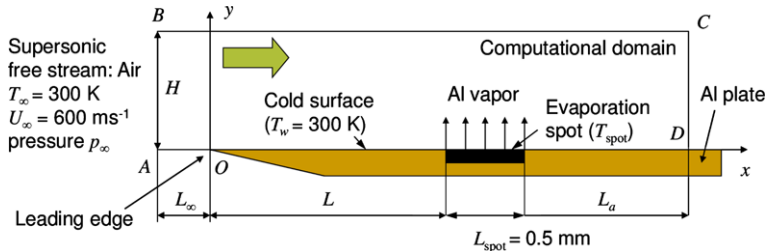
High-power continuous wave (CW) lasers are used in many applications that involve welding, drilling, and cutting of various materials [1]. The process of material removal from the laser spot, usually called laser ablation [2], typically involves melting of the target, evaporation from the laser spot, and expulsion of the molten material under the action of recoil vapor pressure and thermocapillary stresses [3–5]. The material removal can also be assisted and enhanced by an external gas flow generated by a gas jet directed at the laser spot or an unbounded gas stream parallel to the target surface [1, 6, 7]. High-power laser ablation of metal targets in air may result in heterogeneous oxidation of the laser spot and formation of an oxide film on the surface of the molten material. The presence of the oxide film can substantially change the optical, thermal, and mechanical properties of the surface, and thus affect the rate of the material removal [6]. The energy release during exothermal heterogeneous oxidation can also contribute to the thermal energy balance at the surface of the laser spot, and increase the rate of material removal [8].

The interaction between the external gas flow and the evaporating material can limit access of oxygen to the surface of the laser spot, and strongly affect the growth rate of the oxide film [8]. The growth of the oxide film in the oxygen jet-assisted deep laser drilling has been analyzed in simulations that do not account for evaporation of irradiated material, e.g., [8–10] when oxygen can freely diffuse to the oxidized surface. The effect of the interaction between the evaporating material and external high-speed flow, however, has not been investigated yet. In the case of Al targets, the ejection of high-temperature vapor into the air stream can also result in gas-phase combustion of the Al vapor. Chemical reactions in the ablation plume are known to have a strong influence on the dynamics of the ablation products

A.N. Volkov (✉) · L.V. Zhigilei
Department of Materials Science and Engineering, University
of Virginia, 395 McCormick Road, Charlottesville,
VA 22904-4745, USA
e-mail: av4h@virginia.edu

L.V. Zhigilei (✉)
e-mail: lv2n@virginia.edu

Fig. 1 Schematic sketch of the computational setup used in simulations of two-dimensional vapor expansion from a laser (evaporation) spot on an Al plate into a supersonic air flow



[11, 12], and thus can affect the transport of oxygen from the external flow to the laser spot. The deposition of the combustion products on the surface of the target also makes an additional contribution to the growth of the oxide film. A realistic computational description of CW laser ablation of an Al target in the presence of an external air flow, thus is a challenging problem that requires the development of an advanced multiphysics model properly accounting for laser-material interaction, flow of molten material, heterogeneous oxidation and diffusion of oxygen through the oxide film, expansion and burning of the ablation products in an external gas flow, and deposition of the alumina back to the surface of the target.

In this paper, we take the first step in the direction of designing a comprehensive model for simulation of high-power CW laser ablation of Al targets in a supersonic external air flow. The model, described in Sect. 2, represents the interaction of the external air flow and the ablation plume at the kinetic level and is based on the direct simulation Monte Carlo (DSMC) method adopted for simulation of multicomponent chemically reacting mixtures. The model naturally accounts for nonequilibrium effects and diffusive transport of individual species, which are of primary importance in laser induced plumes [12], and enables simulations for a wide range of external gas pressures. The results of the simulations, reported in Sect. 3, reveal that the direct deposition of both oxygen and alumina to the surface of the laser spot is only possible at low values of pressure in the external flow, which correspond to the transitional flow regime with respect to the Knudsen number. At higher values of pressure, in the continuum flow regime, the simulations predict that deposition of both oxygen and alumina occurs only upstream and far downstream the laser spot. In this case, the growth of the alumina film at the laser spot is limited by heterogeneous oxidation of Al at the upstream edge of the laser spot and slow growth of the oxide film in the downstream direction. The summary of the results and future directions in the advancement of the computational model are provided in Sect. 4.

2 Computational model

Computational setup for simulation of a two-dimensional unsteady flow induced by the expansion of Al atomic vapor

from a hot evaporation spot on the surface of a flat Al target into a supersonic external air flow is schematically shown in Fig. 1. The evaporation spot of size L_{spot} represents a spot heated by a CW laser up to a steady-state temperature T_{spot} that corresponds to intense evaporation of the target material. The spot is located at a distance L from the plate leading edge. The rest of the target surface is assumed to have a smaller temperature T_w that corresponds to absence of evaporation. The Al vapor expands into an external supersonic air flow that is characterized by velocity U_∞ , temperature T_∞ , and pressure p_∞ in the free stream that flows in the direction parallel to the target surface. Partial mixing of the high-temperature Al vapor with oxygen from the external flow results in the gas-phase burning of Al and formation of alumina that can deposit back to the target surface. Oxygen can also diffuse through the stream of the evaporating vapor down to the surface of the evaporation spot, leading to the heterogeneous Al oxidation. The setup of the problem has some parallels with the gas dynamics problem of transversal jet expansion into an external supersonic flow, e.g., [13–15].

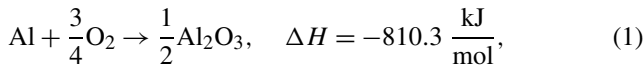
The flow of the multicomponent reactive gas mixture is described at the kinetic level with the DSMC method [16]. In this method, the gas flow is represented by a large number of simulated molecules, which are subject of inelastic binary collisions, chemical reactions, free motion between the collisions, and interaction with the gas-solid/liquid boundaries. A parallel three-dimensional DSMC code previously developed for simulations of the pulsed laser ablation [17] has been adapted in this work for simulations of multicomponent reactive flow. The code is capable of large-scale kinetic simulations of near-continuum flows on thousands of processor cores with hundreds of millions of simulated molecules. In the present paper, the code is used for two-dimensional simulations only.

The chemistry of the gas-phase Al burning is fairly complicated and includes tens of reactions [18, 19]. For many of the reactions, the reaction rates are only known with very large uncertainties [20–22]. The formation of alumina goes through several intermediate Al suboxides and ends by heterogeneous reactions of nucleation and growth of alumina clusters (since alumina does not exist in the gas phase) [21]. The ignition temperature of Al in air depends on the flow conditions and decreases with decreasing size of Al clusters.

For instance, the ignition temperature determined in experiments on combustion of ~ 10 nm Al nanoparticles is as low as 900–1000 K [22, 23]. The maximum flame temperature of the Al burning is limited by the temperature of the endothermic alumina dissociation [21, 24]. The alumina dissociation temperature depends on the partial pressure of Al sub-oxides and, e.g., at pressure 0.1 atm is equal to 3533 K [21].

To the best of our knowledge, the burning of Al vapor-air mixtures has only been studied at continuum level and no comprehensive gas kinetic model of Al combustion has been developed so far. Although both chemical reactions [16, 25, 26] and cluster formation [27–29] can be incorporated into the framework of the DSMC method, the model accounting for the formation and dissociation of Al suboxides would suffer from the lack of reliable data on kinetic parameters of individual reactive collisions. Moreover, an accurate DSMC simulation of a multicomponent reactive mixture, where some of the important species have fairly small molar fractions, requires extremely high number of simulated molecules. This makes simulations of flows at relatively small Knudsen numbers, $Kn_{\infty} = \lambda_{\infty}/L_{\text{spot}} \ll 1$, where λ_{∞} is the mean free path of gas molecules in the free stream, impractical.

In the present work, therefore, the DSMC simulations are performed with a simplified model of Al burning that implies the direct transformation of Al atoms and oxygen molecules into individual “alumina molecules” according to the following reaction [24]:



where ΔH is the heat of combustion of one mole of Al. The number of species in the gas mixture reduces to four, namely, N₂, O₂, Al, and Al₂O₃. Every molecule of species α is assumed to have three translational and ζ_{α} internal (rotational) degrees of freedom. The collisional cross section $\sigma_{\alpha\beta}$ for a collision between molecules of species α and β with the relative velocity c is described by the variable hard sphere model, $\sigma_{\alpha\beta} = \pi d_{\alpha\beta}^2 (c_{\alpha\beta}/c)^{\omega_{\alpha\beta}-1/2}$, where $d_{\alpha\beta}$ is the kinetic molecular diameter at a reference velocity $c_{\alpha\beta}$ and $\omega_{\alpha\beta}$ is the viscosity index. For a reference temperature T_{ref} , the reference velocity in a single-component gas can be calculated as $c_{\alpha\alpha} = \sqrt{2k_B T_{\text{ref}}/m_{\alpha}}/\Gamma^{1/(2\omega_{\alpha\alpha}-1)}(5/2-\omega_{\alpha\alpha})$, where $\Gamma(x)$ is the gamma function, m_{α} is the mass of a molecule of species α , and k_B is the Boltzmann constant [16]. The model parameters for various species are chosen as follows: $M_{\text{O}_2} = 0.032 \text{ kg mol}^{-1}$, $\zeta_{\text{O}_2} = 2$, $d_{\text{O}_2\text{O}_2} = 4.07 \text{ \AA}$, $\omega_{\text{O}_2\text{O}_2} = 0.77$ [16], $M_{\text{N}_2} = 0.028 \text{ kg mol}^{-1}$, $\zeta_{\text{N}_2} = 2$, $d_{\text{N}_2\text{N}_2} = 4.17 \text{ \AA}$, $\omega_{\text{N}_2\text{N}_2} = 0.74$ [16], $M_{\text{Al}} = 0.027 \text{ kg mol}^{-1}$, $\zeta_{\text{Al}} = 0$, $d_{\text{AlAl}} = 4.1 \text{ \AA}$, $\omega_{\text{AlAl}} = 0.8$ [30], and $M_{\text{Al}_2\text{O}_3} = 0.102 \text{ kg mol}^{-1}$, where M_{α} is the molar mass of species α and all $d_{\alpha\alpha}$ are given for $T_{\text{ref}} = 273 \text{ K}$. Since alumina does not exist in molecular form, the kinetic parameters of “alumina molecules” can

only be roughly estimated and are chosen to be $\zeta_{\text{Al}_2\text{O}_3} = 3$, $d_{\text{Al}_2\text{O}_3} = 8 \text{ \AA}$, and $\omega_{\text{Al}_2\text{O}_3} = 0.8$, where the kinetic diameter is estimated as 1.2 of the length of the linear O-Al-O-Al-O chain [31], and the value of the viscosity index is just a characteristic value for many gaseous species [16]. For collisions involving molecules of different species, the parameters are calculated as $d_{\alpha\beta} = (d_{\alpha\alpha} + d_{\beta\beta})/2$, $\omega_{\alpha\beta} = (\omega_{\alpha\alpha} + \omega_{\beta\beta})/2$, and $c_{\alpha\beta} = \sqrt{2k_B T_{\text{ref}}/m_{\alpha\beta}}/\Gamma^{1/(2\omega_{\alpha\beta}-1)}(5/2-\omega_{\alpha\beta})$ at $m_{\alpha\beta} = 2m_{\alpha}m_{\beta}/(m_{\alpha} + m_{\beta})$.

The energy transfer between the translational and internal degrees of freedom during an individual binary collision is described by the Larsen–Borgnakke (LB) model [16, 32] with the collision number equal to unity for all inelastic collisions. The reaction given by Eq. (1) is assumed to not be limited kinetically and is implemented as an additional procedure performed at each time step of the DSMC algorithm. In this procedure, four Al atoms and three O₂ molecules are randomly chosen among the simulated particles in a collision sampling cell and replaced by two “alumina molecules” until the cell does not contain enough particles of the raw species. The translational velocities and internal energies of product “alumina molecules” are sampled at random with the algorithm that corresponds to the LB model and ensures conservation of total momentum and energy, with the latter increased for product species by the heat of reaction, Eq. (1). In subsequent collisions, the “hot” “alumina molecules” transfer their excess energy to other species, so that the mixture gradually evolves to the local thermal equilibrium. Thus, the proposed model correctly accounts for the release of the heat of reaction, but should not be expected to provide a correct description of neither ignition conditions nor the maximum flame temperature.

The evaporation from the hot laser spot is described by the Hertz–Knudsen model [33], which implies a Maxwell–Boltzmann velocity distribution of Al atoms with a given temperature T_{spot} and saturated Al vapor pressure that is determined by the Clausius–Clapeyron equation $p_e(T_{\text{spot}}) = p_0 \exp((L_0 m_{\text{Al}}/k_B)(1/T_0 - 1/T_{\text{spot}}))$, where $L_0 = 10.75 \times 10^6 \text{ J kg}^{-1}$ [2] and $T_0 = 2793 \text{ K}$ [34] are the latent heat of vaporization and boiling temperature at $p_0 = 10^5 \text{ Pa}$. It is assumed that all Al atoms and “alumina molecules” colliding with the surface of the target are absorbed, while the reflection of incident O₂ and N₂ molecules from the surface is described by the Maxwell model of diffuse scattering [35], where the surface relaxation temperature is assumed to be equal to the local surface temperature (either T_w or T_{spot}). Boundary condition of flow symmetry is imposed at the boundary AO (Fig. 1), while at the entrance AB, top BC, and exit CD sides of the computational domain the inflow of N₂ and O₂ molecules is described by the Maxwell–Boltzmann distribution with U_{∞} , T_{∞} , and p_{∞} . Molecules leaving the computational domain through these boundaries

are excluded from the consideration. In all simulations, the size of the computational system is chosen to be sufficiently large to prevent the influence of the positions of boundaries AB , BC , and CD on the gas flow between the leading edge and the laser spot, as well as in the immediate vicinity of the laser spot. In particular, a series of auxiliary simulations is performed, when the boundary positions are varied as follows: $L_\infty/L_{\text{spot}} = 0.05–10$, $L_a/L_{\text{spot}} = 5–15$, and $H/L_{\text{spot}} = 5–20$. Based on these simulations, values of L_∞ , L_a , and H are chosen for final simulations, which ensure the independence of the flow structure on further increase in L_∞ , L_a , and H in the domain shown in Figs. 2–7.

The pressure in the free stream, p_∞ , and the laser spot temperature T_{spot} are varied in the simulations within the ranges $p_\infty = 50–10000$ Pa and $T_{\text{spot}} = 2041–2793$ K (corresponds to $p_e = 10^3–10^5$ Pa). The laser spot temperature can be related to the irradiation conditions with the help of the one-dimensional thermal model of [17] that accounts for CW laser heating of Al target, heat conduction, and evaporation from the surface. The calculations performed with this model show that the surface temperatures considered in the simulations can be achieved at absorbed intensities of laser irradiation ranging from 6×10^6 to 6×10^8 W m $^{-2}$ or incident intensities ranging from 2×10^8 to 2×10^{10} W m $^{-2}$ (estimated for reflectivity of 0.97 [2]). With a proper focusing of the laser beam, such intensities can be achieved even with a compact CW laser system based, e.g., on a single-mode fiber laser [36]. All other model parameters are assumed to have constant values as follows: Mole fractions of O₂ and N₂ in the free stream are equal to $x_{O_2\infty} = 0.21$ and $x_{N_2\infty} = 0.79$, $T_\infty = T_w = 300$ K, $U_\infty = 600$ m s $^{-1}$. The corresponding Mach number is $Ma_\infty = U_\infty / \sqrt{\gamma_{\text{Air}} R_{\text{Air}\infty} T_\infty} = 1.73$, where $\gamma_{\text{Air}} = 1.4$ and $R_{\text{Air}\infty} = k_B / (m_{O_2} x_{O_2\infty} + m_{N_2} x_{N_2\infty}) = 288$ J kg $^{-1}$ K $^{-1}$ are the specific heat ratio and the gas constant of air.

The effects of rarefaction and nonequilibrium under the simulated conditions are characterized by the Knudsen number $Kn_\infty = \lambda_\infty / L_{\text{spot}}$. The value of λ_∞ is calculated based on a simplified equation for single-component gas of hard sphere molecules, $\lambda_\infty = (\sqrt{2\pi} d_{\text{Air}} (n_{O_2\infty} + n_{N_2\infty}))^{-1}$, where $d_{\text{Air}} = 4.19$ Å [16] and $n_{\alpha\infty}$ is the number density of species α in the free stream. The pressure range considered in this work corresponds to the transitional ($Kn_\infty \sim 1$) and continuum ($Kn_\infty \ll 1$) flow regimes. In the majority of the simulations, both p_∞ and T_{spot} are varied simultaneously in order to reveal the effect of Kn_∞ at a fixed value of the momentum flux ratio $J = \gamma_{\text{Al}} p_e(T_{\text{spot}}) Ma_e^2 / (\gamma_{\text{Air}} p_\infty Ma_\infty^2)$. Here, $\gamma_{\text{Al}} = 5/3$ is the specific heat ratio for Al vapor and Ma_e is the Mach number at the spot surface that can be estimated as $Ma_e = U_e / \sqrt{\gamma_{\text{Al}} k_B T_{\text{spot}} / m_{\text{Al}}} = \sqrt{6/(5\pi)} \approx 0.62$, where $U_e = \sqrt{2k_B T_{\text{spot}} / (\pi m_{\text{Al}})}$ is the macroscopic velocity of vapor at the spot surface calculated with the Hertz-Knudsen model under assumption of zero flux of atoms returning back to the surface. The momentum ratio is known

to be the key parameter that governs the flow structure in a similar problem of transversal jet expansion into external flow in the continuum regime [37]. In particular, the characteristic penetration height of the jet in this regime is found to be mostly defined by J [15].

The elements of the computational setup shown in Fig. 1 have the following dimensions: $L_{\text{spot}} = 0.5$ mm, $L / L_{\text{spot}} = 14.6$, $L_a = 5.2$ mm, $L_\infty = 0.1–4$ mm, and $H = 4.5–9$ mm. The values of L_∞ and H used in simulations are increased with increasing Kn_∞ in order to account for the decreasing collision frequency that allows the Al atoms to diffuse over larger distances from the spot in the upstream and normal to the surface directions. The DSMC simulations are performed on a homogeneous Cartesian mesh of square cells used for collision sampling with the cell size of 0.5 to 10 μm and the time step of 0.2 to 2 ns. The number of simulated molecules in a cell located in the free stream is varied from 6 to 100. The total number of simulated molecules in the simulations, e.g., at $Kn_\infty = 0.0022$, is equal to about 10^9 . The numerical parameters are adjusted for each Kn_∞ in order to provide an accurate description of the Knudsen layer at the target surface. In order to capture unsteady features of the flow, which are characteristic for transversal jet expansion [14, 37], the spatial distributions of macroscopic flow parameters are calculated every microsecond by averaging local molecular parameters over 0.2–0.4 μs. This time averaging decreases the level of statistical scattering of local parameters, but does not significantly affect the time-dependant features of quasiperiodic flows that evolve at much longer timescales, with the characteristic periods of flow oscillations ranging from tens to hundreds of μs. The distributions of macroscopic gas parameters obtained in the averaging procedure are, therefore, referred to as “instantaneous” (to distinguish them from distributions where quasiperiodic oscillations are removed by time-averaging over longer periods of time) in the description of the results below. In order to ensure the numerical convergence, the mixture pressure is calculated in a few points evenly distributed along the target surface, and the flows are simulated until the magnitudes of the pressure oscillations in these points remain constant during two–three successive periods of oscillation.

The formation of an ablation crater at the target surface is not considered in simulations, since its effect on the mixture flow at the initial stage of the ablation process is small. At the highest laser spot temperature considered in simulations, $T_{\text{spot}} = 2793$ K, the surface recession rate due to the evaporation, estimated assuming zero flux of back-scattered Al atoms, $\Phi = p_e(T_{\text{spot}}) / \sqrt{2\pi k_B T_{\text{spot}} / m_{\text{Al}}} / \rho_{\text{Al}}$ ($\rho_{\text{Al}} = 2700$ kg m $^{-3}$ is the Al density), is equal to 0.016 mm ms $^{-1}$. Thus, during the initial ~ 10 ms, the crater remains relatively shallow and the effect of the evolving surface geometry can

be neglected. It is worth noting that the steady or quasiperiodic state of the mixture flow is established in the simulations on a much shorter (tens to hundreds of μs) time scale.

3 Results and discussion

For each set of simulation parameters, the flow of chemically inert mixture is first calculated for 100–400 μs with the part of the algorithm responsible for sampling of chemical reactions switched off. When the flow reaches a steady or quasiperiodic state (Fig. 2), the simulation continues with the oxidation reaction described by Eq. (1) turned on for additional 100–200 μs until a new steady state or quasiperiodic state is achieved (Fig. 3). Such an approach is used in order to identify the effect of oxidation on the flow structure. Below, the computational results are first considered for chemically-inert flow in order to identify the basic flow features and regimes in the range of the external gas pressure considered in this work. Next, the effect of the Al vapor burning on the flow structure is discussed. Finally, the deposition of alumina to the surface of the irradiated target and different scenarios of the formation of alumina film within the laser spot are considered in different flow regimes.

In chemically inert flows, simulations predict a pronounced effect of the external gas pressure on the flow structure that is mainly determined by the flow Knudsen number Kn_∞ (Fig. 2). At relatively large Kn_∞ (e.g., $Kn_\infty = 0.22$), which correspond to the transitional flow regime, flows are steady-state (within the computational error and statistical noise intrinsic to DSMC simulations) and are characterized by the absence of vortex regions and distinct shock waves, Fig. 2a. Due to relatively large values of the molecular mean free path, the disturbances introduced into the free stream by the plate and the expanding Al vapor propagate some distance upstream the plate leading edge located at $x = 0$. At smaller Kn_∞ , a boundary layer tends to form in a region between the plate leading edge and the evaporation spot, while the expansion of Al vapor induces the separation of the boundary layer from the plate and the formation of a region with circulating flow upstream the evaporation spot. The separation point is located in a close vicinity of the plate leading edge in Figs. 2b and 2c, but shifts downstream from the leading edge for smaller J or larger L/L_{spot} . At $Kn_\infty = 0.022$, when the flow occurs in the continuum regime, the separation of the boundary layer, formation of a circulating flow region with two circulation zones, and generation of a separation shock wave are observed, although the flow remains steady state within the level of statistical noise. Further decrease in Kn_∞ , down to 0.0022, results in the formation of multiple circulation zones and bow shocks, as well as in pronounced oscillations of the whole flow structure, Fig. 2c. In simulations performed at smaller Knudsen numbers, $Kn_\infty = 0.0011$ with

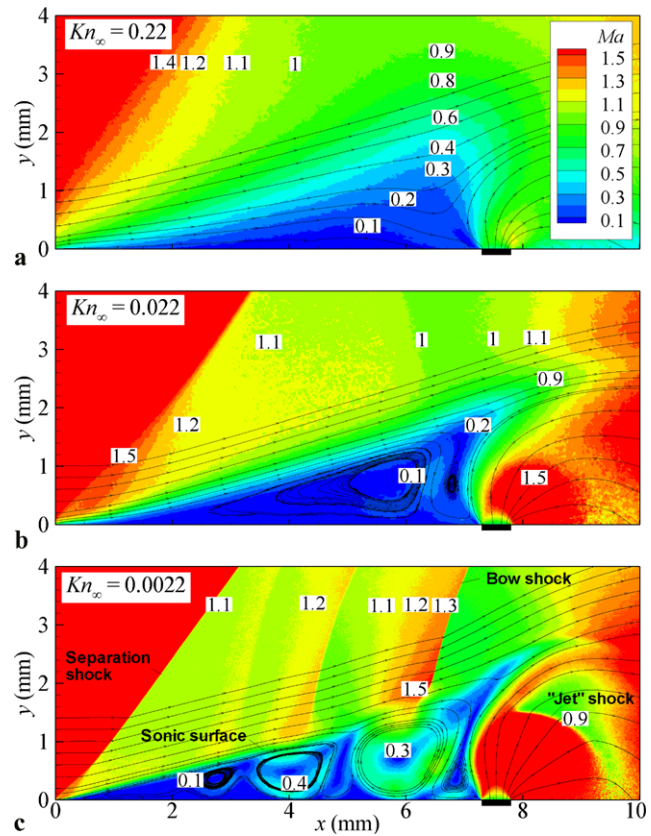


Fig. 2 Instantaneous fields of local Mach number Ma and stream line patterns in the flows of chemically inert mixture at $p_\infty = 50 \text{ Pa}$, $T_{\text{spot}} = 2041 \text{ K}$ (a, $Kn_\infty = 0.22$), $p_\infty = 500 \text{ Pa}$, $T_{\text{spot}} = 2358 \text{ K}$ (b, $Kn_\infty = 0.022$), and $p_\infty = 5000 \text{ Pa}$, $T_{\text{spot}} = 2793 \text{ K}$ (c, $Kn_\infty = 0.0022$) for $Ma_\infty = 1.73$, $L/L_{\text{spot}} = 14.6$, and $J = 3.04$. The evaporation spot is marked by the black rectangle. The Mach number Ma is defined as $Ma = U_{\text{Mix}}/\sqrt{2\gamma_{\text{Mix}}E_{t,\text{Mix}}/(3\rho_{\text{Mix}})}$, where U_{Mix} , ρ_{Mix} , and $E_{t,\text{Mix}}$ are the local mixture velocity, mass density, and translational thermal energy density, $\gamma_{\text{Mix}} = (5 + \zeta_{\text{Mix}})/(3 + \zeta_{\text{Mix}})$, ζ_{Mix} is the local average value of internal degrees of freedom per particle of the mixture

$J = 1.52$ and $Kn_\infty = 0.0005$ with $J = 0.76$ (in both cases $T_{\text{spot}} = 2973 \text{ K}$ and $p_e = 10^5 \text{ Pa}$), the intermediate bow shocks disappear and the flow structure resembles the one observed for a two-dimensional transversal continuum jet expanding into a supersonic free stream, e.g., [13, 15]. An important distinction of the conditions considered in this work as compared to the ones in [13, 15], however, is that a complete adsorption of Al atoms colliding with the surface is assumed in the present model, whereas no condensation at the surface of the plate is present in the simulations of the transversal jet expansion [13, 15]. This results in qualitative differences in the structure of the expanding vapor jets at small Kn_∞ . Although the subsonic flow at the surface ($Ma_e < 1$) rapidly accelerates to supersonic speeds, the “barrel” structure with the Mach disk that is characteristic of underexpanded jets [13, 15] is not formed in Fig. 2c. Instead, the Mach disk in the vapor jet is replaced by a curved shock

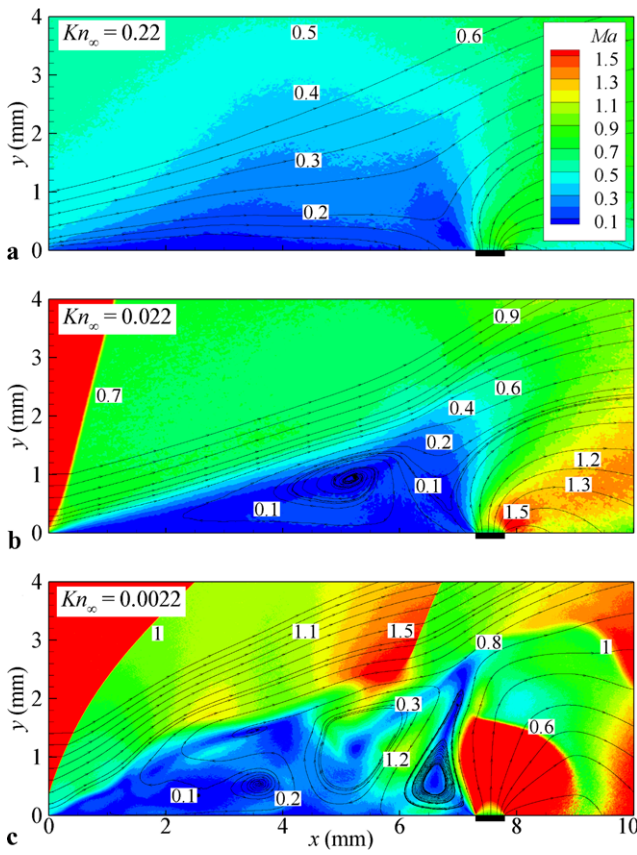


Fig. 3 Instantaneous fields of local Mach number Ma and stream line patterns in the flows of burning mixture at $p_{\infty} = 50$ Pa, $T_{\text{spot}} = 2041$ K (a, $Kn_{\infty} = 0.22$), $p_{\infty} = 500$ Pa, $T_{\text{spot}} = 2358$ K (b, $Kn_{\infty} = 0.022$), and $p_{\infty} = 5000$ Pa, $T_{\text{spot}} = 2793$ K (c, $Kn_{\infty} = 0.0022$) for $Ma_{\infty} = 1.73$, $L/L_{\text{spot}} = 14.6$, and $J = 3.04$. The evaporation spot is marked by the black rectangle

wave that encloses the supersonic part of the expanding Al vapor. A region of highly rarefied flow, which is formed right behind the evaporation spot, induces a significant increase in the thickness of the shock front that becomes smeared closer to the surface.

In chemically reacting flows (Fig. 3), the simulations at $Kn_{\infty} = 0.22$ and $Kn_{\infty} = 0.022$ predict flow structures that are similar to those of corresponding chemically inert flows. At $Kn_{\infty} = 0.0022$, the burning of Al vapor results in the formation of an essentially unsteady flow structure, where the positions and shapes of the separation and bow shocks vary with time. In this case, during the simulation time from ~ 40 μ s to ~ 100 μ s after the oxidation reaction is “turned on,” the flow structure exhibits cyclic changes illustrated in Fig. 4. During a cycle, initially “thick” circulating zone with complex, irregular flow (Fig. 4a) is rapidly taken away by the external flow and gives way to a new circulating zone developing between the leading edge and the spot (Fig. 4b). The growing circulating zone eventually becomes unstable (Fig. 4c) and evolves into a new zone of irregular flow (Fig. 4d). The characteristic frequency of these large-scale

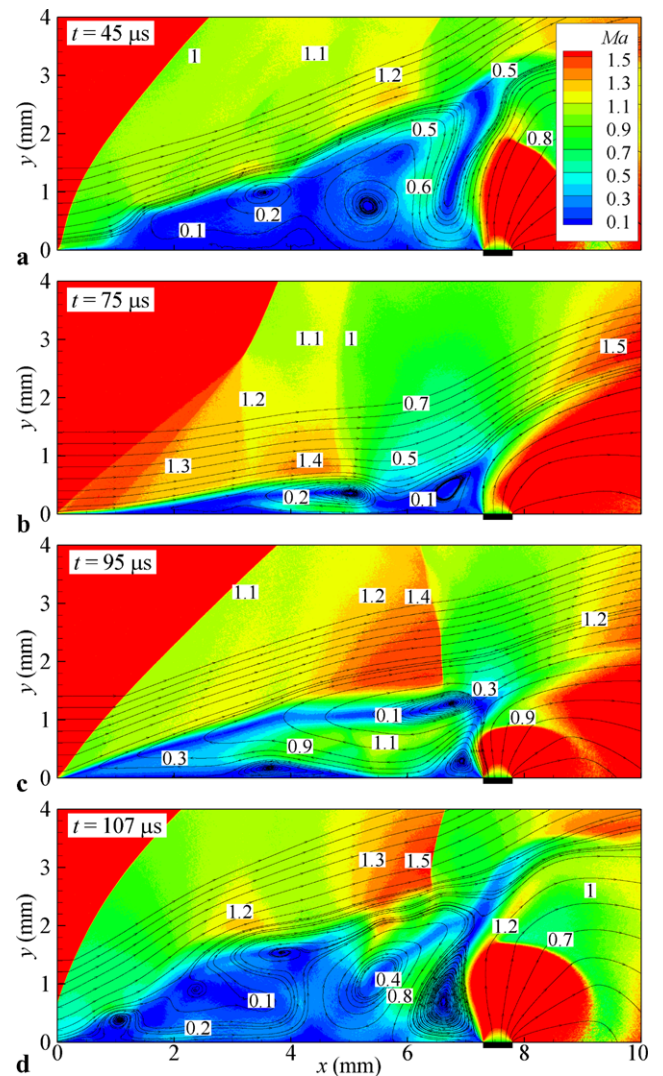


Fig. 4 Instantaneous fields of local Mach number Ma and stream line patterns in the flow of burning mixture at $p_{\infty} = 5000$ Pa, $T_{\text{spot}} = 2793$ K ($Kn_{\infty} = 0.0022$), $Ma_{\infty} = 1.73$, $L/L_{\text{spot}} = 14.6$, and $J = 3.04$ obtained at time 45 μ s (a), 75 μ s (b), 95 μ s (c), and 107 μ s (d) after “turning on” the oxidation reaction, Eq. (1), in the initial flow of chemically inert mixture shown in Fig. 2c. The fields in Figs. 3c, 6c, and 7c are obtained at time 105 μ s in the same simulation. The evaporation spot is marked by the black rectangle

oscillations is ~ 20 kHz. Although the magnitude of the flow oscillations may continue to evolve after the first cycle, the simulation was not extended to longer times to avoid an excessive use of limited computational resources.

The basic quantitative difference between the chemically inert and reacting flows is that the heat released due to the Al burning increases pressure in the flow region between the leading edge of the plate and the evaporation spot. In the transitional flows ($Kn_{\infty} = 0.22$), this pressure increase results in the expansion of the region of disturbed flow upstream the plate leading edge (the region of undisturbed free stream is not present in Fig. 3a). In continuum flows, the

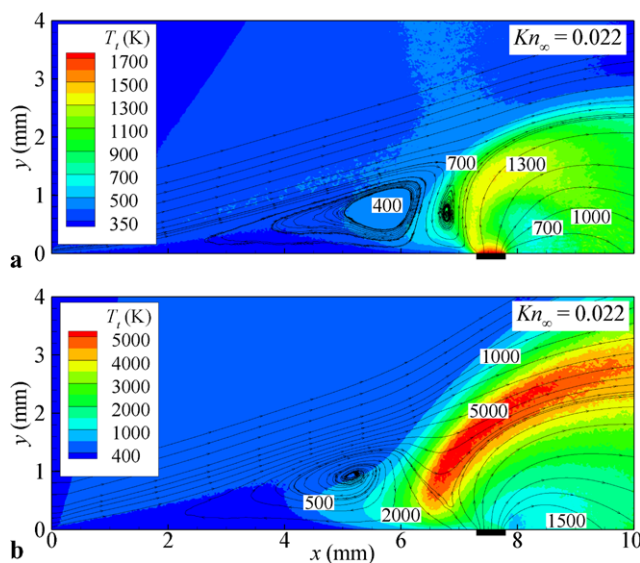


Fig. 5 Instantaneous fields of translational temperature T_t in the flows of chemically inert (a) and burning (b) mixtures at $p_\infty = 500$ Pa, $T_{\text{spot}} = 2358$ K ($Kn_\infty = 0.022$), $Ma_\infty = 1.73$, $L/L_{\text{spot}} = 14.6$, and $J = 3.04$. The evaporation spot is marked by the black rectangle

release of heat results in the increase in the angle of the oblique separation shock with respect to the free stream direction (Fig. 3b) or formation of a curved separation shock (Fig. 3c).

In the flow of chemically-reacting mixture, the flame zone can be approximately identified as a zone of elevated temperature. The analysis of the fields of translational temperature (Fig. 5b) shows that the flame zone is located in the mixing layer separating the external flow and the expanding Al vapor. Since the reaction of alumina decomposition is not included in the model, the temperature in the flame zone may exceed the dissociation temperature of the alumina. The observation that the maximum temperature in Fig. 5b is indeed substantially higher than the dissociation temperature of alumina implies that the results of the simulations can only provide an upper bound estimate of the rate of alumina formation. On the other hand, in all flows of chemically-inert mixtures considered in this paper, the temperature in the Al vapor–air mixing layer at the boundary between the external flow and the Al vapor exceeds 1000 K (e.g., Fig. 5a), which is sufficient, according to data on Al nanoparticle combustion [22, 23], for ignition and burning of Al vapor.

It is seen from Fig. 5b that the flame zone is located relatively close to the target surface, so that the Al burning can rise the gas temperature near the surface in excess of 2000 K within a relatively large ($\sim 2L_{\text{spot}}$ in Fig. 5b) region upstream the laser spot. The formation of such high-temperature region near the surface is a common feature of all simulations of reactive flows considered in this paper. In the transitional flows at large Knudsen numbers, e.g., at $Kn_\infty = 0.22$, the gas temperature rises at both sides of

the evaporation spot. The exposure of the target surface to high-temperature gas mixtures can induce melting and even heterogeneous burning of Al, leading to additional target damage and material removal outside the laser spot. Although this effect can not be described quantitatively with the current model, the simulations suggest a potentially pronounced effect of additional target heating due to the gas-phase Al burning.

The processes responsible for the formation of alumina film on the surface of the evaporation spot at various pressures of the external flow can be identified from analysis of instantaneous fields of number density of oxygen (Fig. 6) and alumina (Fig. 7) in the reactive flows as well as the distributions of number fluxes of oxygen and alumina incident to the plate surface (Fig. 8). At $Kn_\infty = 0.22$, the diffusive mixing and reactive interaction of Al and O₂ result in the formation of a large region with substantial density of alumina that extends in both upstream and downstream directions with respect to the evaporation spot. The number density of oxygen, however, drops inside this region by two–three orders of magnitude as compared to the oxygen density in the free stream, $n_{O_2\infty} = 2.82 \times 10^{23}$ m⁻³. The number flux of oxygen molecules incident to the surface, F_{O_2} , approaches a value $\sim 2 \times 10^{21}$ m⁻² s⁻¹ at the edge of the evaporation spot, which is in almost two orders of magnitude smaller than the number flux of oxygen incident to the surface from the undisturbed free stream, $F_{O_2\infty} = n_{O_2\infty}\sqrt{k_B T_\infty/(2\pi m_{O_2})}$, shown by the red dashed line in Fig. 8a. The incident flux of alumina, $F_{Al_2O_3}$, in the center of the spot is equal to 10²² m⁻² s⁻¹, i.e., more than five times larger than the oxygen flux. This flux corresponds to the growth rate of alumina film equal to $m_{Al_2O_3} F_{Al_2O_3}/\rho_{Al_2O_3} = 0.446 \mu\text{m s}^{-1}$ ($\rho_{Al_2O_3} = 3800 \text{ kg m}^{-3}$ is the alumina density [5]). Thus, in the transitional flow regime, the formation of an alumina film on the surface of the evaporation spot is dominated by direct deposition of alumina formed by the gas-phase burning of Al vapor.

In continuum flows at smaller Kn_∞ , the effect of diffusion drops, leading to the decrease in the thickness of the region of high density of alumina. At $Kn_\infty = 0.022$ and $Kn_\infty = 0.0022$, the alumina cannot diffuse through the expanding vapor of Al to the surface of the spot, but is carried away by the Al vapor away from the spot. These alumina can only be deposited to the surface far beyond the spot (green curve at $x \geq 10$ mm in Fig. 8b). A fraction of alumina formed in the flame zone is trapped in the circulation zone and can be transported far upstream the spot (Figs. 7b and 7c). Although the formation of new alumina in the circulation region does not occur due to the lack of available Al atoms, the number density of alumina trapped in this region is high and increases with reduction of Kn_∞ from 0.022 to 0.0022, Figs. 7b and 7c. This results in a substantial incident flux of alumina to the part of the surface below the circulation zone. A relatively high level of statistical noise

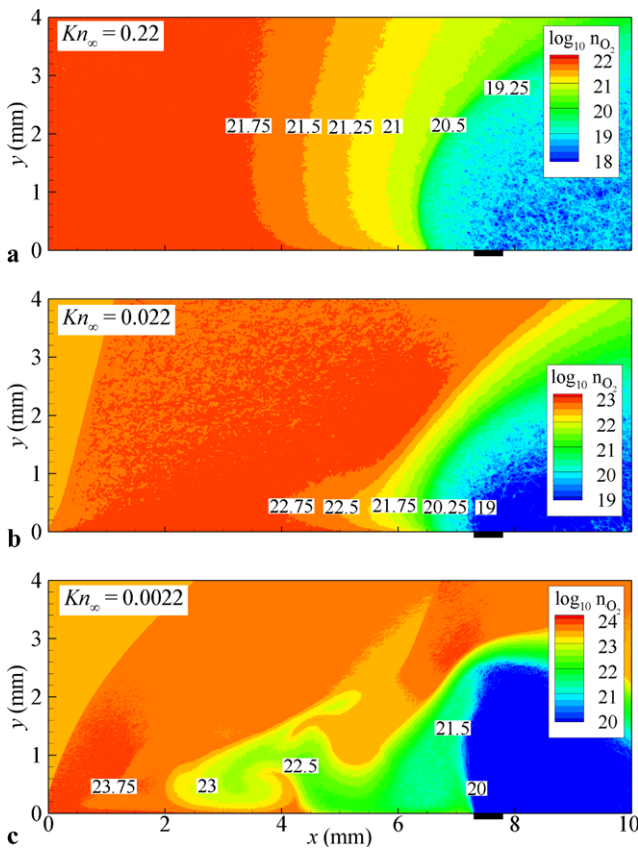


Fig. 6 Instantaneous fields of oxygen number density n_{O_2} (m^{-3}) in the flows of burning mixture at $p_\infty = 50$ Pa, $T_{\text{spot}} = 2041$ K (a, $Kn_\infty = 0.22$), $p_\infty = 500$ Pa, $T_{\text{spot}} = 2358$ K (b, $Kn_\infty = 0.022$), and $p_\infty = 5000$ Pa, $T_{\text{spot}} = 2793$ K (c, $Kn_\infty = 0.0022$) for $Ma_\infty = 1.73$, $L/L_{\text{spot}} = 14.6$, and $J = 3.04$. The evaporation spot is marked by the black rectangle

in this region at $Kn_\infty = 0.0022$ makes an accurate calculation of the time-dependent distribution of alumina deposition flux difficult. This flux, however, abruptly drops at the upstream edge of the spot. At $Kn_\infty = 0.022$, $F_{Al_2O_3}$ is equal to $3 \times 10^{22} m^{-2} s^{-1}$ at distance of ~ 0.02 mm upstream the spot, but no alumina is deposited directly to the spot itself. Similarly, the oxygen flux at the same distance upstream the spot has the same order of magnitude, about $(1-4) \times 10^{22} m^{-2} s^{-1}$ (more accurate determination is not possible due to the statistical noise), but no oxygen incident to the surface of the spot is observed. At $Kn_\infty = 0.0022$, both F_{O_2} and $F_{Al_2O_3}$ drop to zero at the upstream edge of the spot, but the characteristic feature of this case is a relatively large value of F_{O_2} very close to the edge of the spot. For instance, at a distance of 0.03 mm from the spot $F_{O_2} \approx 10^{25} m^{-2} s^{-1}$, which is only about three times smaller than $F_{O_2\infty}$, whereas $F_{Al_2O_3}$ is one to two orders of magnitude smaller than F_{O_2} . In this case, the distributions of both incident fluxes, F_{O_2} and $F_{Al_2O_3}$, are subject of time-dependant variations due to large-scale cycling changes in the flow field demonstrated in Fig. 4. In the region close to

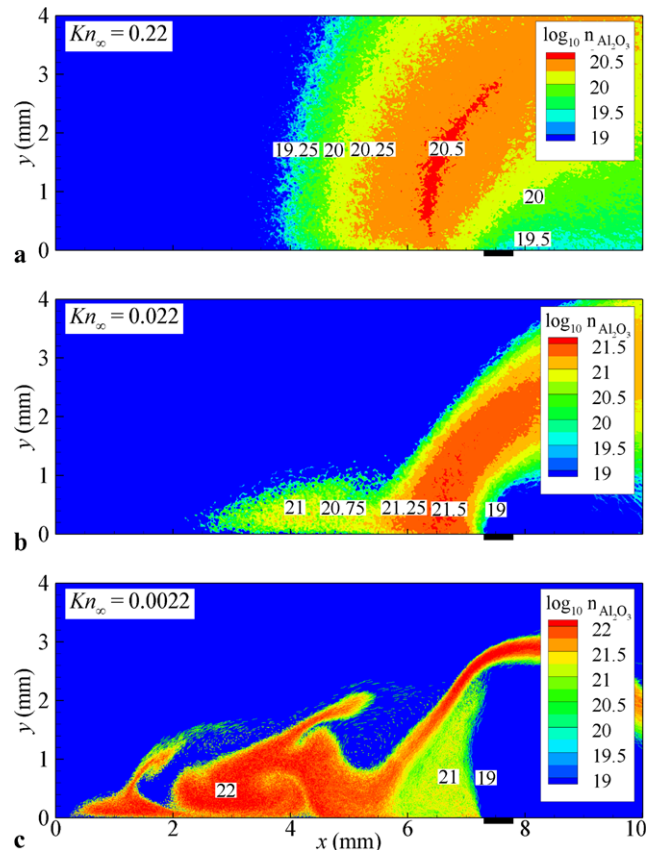


Fig. 7 Instantaneous fields of alumina number density $n_{Al_2O_3}$ (m^{-3}) in the flows of burning mixture at $p_\infty = 50$ Pa, $T_{\text{spot}} = 2041$ K (a, $Kn_\infty = 0.22$), $p_\infty = 500$ Pa, $T_{\text{spot}} = 2358$ K (b, $Kn_\infty = 0.022$), and $p_\infty = 5000$ Pa, $T_{\text{spot}} = 2793$ K (c, $Kn_\infty = 0.0022$) for $Ma_\infty = 1.73$, $L/L_{\text{spot}} = 14.6$, and $J = 3.04$. The evaporation spot is marked by the black rectangle

the spot (2–3 mm upstream the spot), F_{O_2} and $F_{Al_2O_3}$ vary in time within the order of magnitude. The distributions shown in Fig. 8 approximately correspond to the time when both fluxes are minimal in this region.

In contrast to the results of CW laser cutting simulations of [8], where the heterogeneous oxidation of the irradiated surface was considered under assumption of the absence of the evaporation, the present simulations show that strong evaporation in the continuum flow regime prevents the gas-phase diffusion from delivering oxygen to the laser spot. It is worth noting that simulations of chemically inert flows cannot predict correct values of the oxygen flux in the vicinity of the evaporation spot (thin black curved in Fig. 8a) and, therefore, cannot be used for calculation of heterogeneous Al oxidation. For instance, at $Kn_\infty = 0.22$ and $Kn_\infty = 0.022$, the values of F_{O_2} near the evaporation spot are one to two orders of magnitude larger in the flows of chemically inert mixtures as compared to the corresponding fluxes in the flows of burning Al vapor.

In the range of Kn_∞ considered in this paper, the maximal values of F_{O_2} are approximately proportional to $n_{O_2\infty}$,

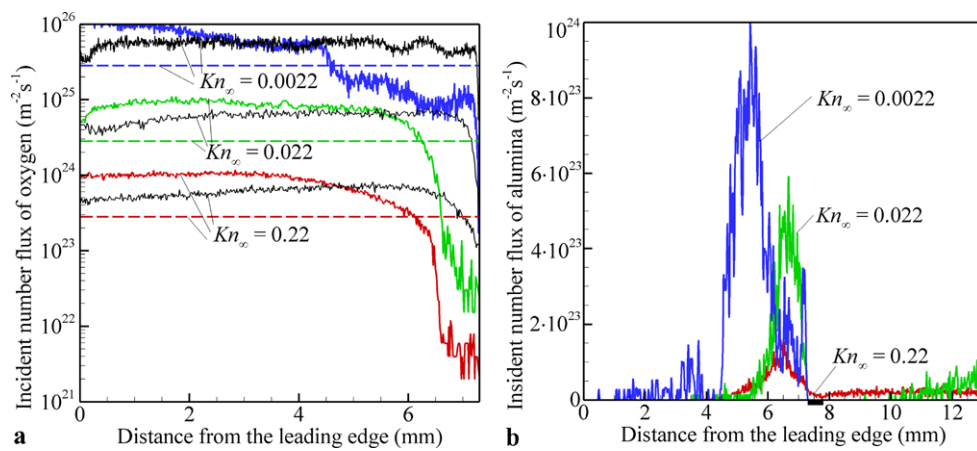


Fig. 8 Distributions of incident number fluxes of oxygen (**a**) and alumina (**b**) along the target surface in the flow of burning mixture at $p_\infty = 50$ Pa, $T_{\text{spot}} = 2041$ K (red solid curves, $Kn_\infty = 0.22$), $p_\infty = 500$ Pa, $T_{\text{spot}} = 2358$ K (green solid curves, $Kn_\infty = 0.022$), and $p_\infty = 5000$ Pa, $T_{\text{spot}} = 2793$ K (blue solid curves, $Kn_\infty = 0.0022$) for $Ma_\infty = 1.73$, $L/L_{\text{spot}} = 14.6$, and $J = 3.4$. Dashed

lines in panel **a** show the number flux of oxygen in the free stream, $n_{O_2\infty}\sqrt{k_B T_\infty}/(2\pi m_{O_2})$. Thin black curves in panel **a** correspond to the number flux of oxygen incident to the target surface in the flows of chemically inert mixture. Instantaneous distributions in the burning mixture at $Kn_\infty = 0.0022$ and the fields shown in Figs. 6c and 7c correspond to the same time of 105 μs in the simulation

whereas the maximum values of $F_{\text{Al}_2\text{O}_3}$ have much weaker dependences on $n_{O_2\infty}$. Namely, an increase of $n_{O_2\infty}$ by two orders of magnitude results only in about 8-fold increase of $F_{\text{Al}_2\text{O}_3}$. The dependence of the distribution of $F_{\text{Al}_2\text{O}_3}$ at the surface upstream the spot on Kn_∞ is defined by two counteracting factors. First, the formation and expansion of a circulating flow region with decreasing Kn_∞ results in the entrapment of alumina in the circulation zones and its transport in the upstream direction. The entrapment is likely to be augmented by the transition to unsteady, quasicirculating flow regime observed upon further decrease of Kn_∞ . Second, the decrease in Kn_∞ reduces the extent of diffusive mixing and results in enhanced transport of alumina from the flame zone in the downstream direction.

Unlike the well-defined constant temperature evaporation spot, assumed in the simulations, the intensity of laser irradiation in CW laser ablation experiments typically has a Gaussian spatial profile and decreases from the center to the periphery of the spot. The central region with active evaporation, therefore, can be expected to be surrounded by colder melted periphery with low Al vapor pressure. In this case, the melted periphery will be exposed to oxidation and deposition of alumina (high F_{O_2} and $F_{\text{Al}_2\text{O}_3}$), leading to the formation of alumina film and possible diffusive-convective transport of alumina in the molten material from the upstream edge of the spot in the downstream direction.

4 Summary

The application of a state-of-the-art DSMC method to investigation of CW laser ablation of an Al target in the presence of an external supersonic air flow reveals two possible

scenarios of the alumina film formation at and around the laser spot. At small pressure in the external flow, when the Knudsen number is relatively large and the transitional flow regime is realized, the molecular diffusion is responsible for transport of alumina and oxygen to the spot through the stream of evaporating material. In this regime, the growth of the oxide film on the surface of the laser spot is dominated by heterogeneous oxidation of the melted Al and direct deposition of alumina formed through gas-phase reactions. The simulations based on a simplified model of Al combustion, Eq. (1), suggest that the number flux of alumina to the surface of the spot is much larger than that of oxygen, so that the growth or alumina film is likely to be dominated by the alumina deposition in this regime. This conclusion, however, needs to be verified in simulations performed with a model accounting for finite reaction rates and dissociation of alumina at high temperatures.

At large pressure in the external flow and small Knudsen numbers, when the continuum flow regime is realized, the molecular diffusion is found to be unable to deliver neither oxygen nor alumina directly to the spot surface. Instead, a fraction of alumina formed in the flame zone is captured by large-scale vortex motion occurring in the separation region upstream the evaporation spot. The convection in the separation region can also efficiently transport oxygen to the upstream edge of the spot. In this regime, the simulations suggest a fairly complicated scenario of the alumina film formation. It includes deposition of alumina trapped in the circulation zones upstream the evaporation spot, effective delivery of oxygen to the upstream edge of the evaporation spot, and possible growth of alumina film from the upstream edge of the spot in the downstream direction. The rate of the direct

deposition of alumina formed in the gas-phase burning of Al vapor in this case appears to be very small. The burning of Al vapor, however, plays an important role in defining the flow structure upstream the evaporation spot and, therefore, the rates of oxygen and alumina deposition in the vicinity of the upstream edge of the spot.

Simulations also suggest a potentially strong contribution of the heat released in the flame zone to heating and melting of the target material outside the laser spot. The quantitative characterization of this and some of the other aspects of the ablation phenomenon, however, requires further advancement of the computational model. The DSMC simulation of the complex flow patterns considered in this work should be coupled with hydrodynamic modeling of melt expulsion under the action of recoil vapor pressure, thermo-capillary stresses, and shear stresses from the external gas flow, thermal modeling of the heat transfer and melting in the irradiated target, and more accurate representation of gas-phase and heterogeneous chemical reactions. The simulations reported in this paper reveal the flow regimes and key processes responsible for the alumina formation, and suggest that the DSMC method provides a solid framework for the development of a more advanced multi-physics computational model for simulation of CW laser ablation in an external air flow.

Acknowledgements Financial support for this work is provided by the Air Force Office of Scientific Research (Grant FA9550-10-1-0541). Computational support is provided by the Oak Ridge Leadership Computing Facility (project MAT009) and the National Science Foundation through the Extreme Science and Engineering Discovery Environment (project TG-DMR110090).

References

1. J. Dowden (ed.), *The Theory of Laser Materials Processing. Heat and Mass Transfer in Modern Technology*. Springer Series in Materials Science, vol. 119 (Springer, Berlin, 2009)
2. D. Bäuerle, *Laser Processing and Chemistry* (Springer, Berlin, 2000)
3. V. Semak, A. Matsunawa, *J. Phys. D, Appl. Phys.* **30**, 2541 (1997)
4. B.S. Yilbas, S.B. Mansoor, *J. Phys. D, Appl. Phys.* **39**, 3863 (2006)
5. S.P. Harimkar, A.N. Samant, N.B. Dahotre, *J. Appl. Phys.* **101**, 054911 (2007)
6. K.C.A. Crane, R.K. Garnsworthy, L.E.S. Mathias, *J. Appl. Phys.* **51**, 5954 (1980)
7. C.D. Boley, K.P. Cutter, S.N. Fuchs, P.H. Pax, M.D. Rotter, A.M. Rubenchik, R.M. Yamamoto, *J. Appl. Phys.* **107**, 043106 (2010)
8. K. Chen, Y.L. Yao, V. Modi, *Int. J. Adv. Manuf. Technol.* **15**, 835 (1999)
9. D. Schuöcker, *Appl. Phys. B* **40**, 9 (1986)
10. G.V. Ermolaev, O.B. Kovalev, *J. Phys. D, Appl. Phys.* **42**, 185506 (2009)
11. T.E. Itina, V.N. Tokarev, W. Marine, M. Autric, *J. Chem. Phys.* **106**, 8905 (1997)
12. M. Capitelli, A. Casavola, G. Colonna, A. De Giacomo, *Spectrochim. Acta B* **59**, 271 (2004)
13. C.E. Glass, G.J. LeBeau, AIAA paper 97-2536 (1997)
14. V. Viti, R. Neel, J.A. Schetz, *Phys. Fluids* **21**, 046101 (2009)
15. E. Erdem, K. Kontis, *Shock Waves* **20**, 103 (2010)
16. G.A. Bird, *Molecular Gas Dynamics and the Direct Simulation of Gas Flows* (Clarendon Press, Oxford, 1994)
17. A.N. Volkov, G.M. O'Connor, T.J. Glynn, G.A. Lukyanov, *Appl. Phys. A* **92**, 927 (2008)
18. M.T. Swihart, L. Catoire, *Combust. Flame* **121**, 210 (2000)
19. E.B. Washburn, J.N. Trivedi, L. Catoire, M.W. Beckstead, *Combust. Sci. Technol.* **180**, 1502 (2008)
20. L. Catoire, J.-F. Legendre, M. Giraud, *J. Propuls. Power* **19**, 196 (2003)
21. M.W. Beckstead, Y. Liang, K.V. Pudduppakkam, *Combust. Explos. Shock Waves* **41**, 622 (2005)
22. Y. Huang, G.A. Risha, V. Yang, R.A. Yetter, *Combust. Flame* **156**, 5 (2009)
23. T. Bazyn, H. Krier, N. Glumac, *Combust. Flame* **145**, 703 (2006)
24. K. Benkiewicz, A.K. Hayashi, *Fluid Dyn. Res.* **30**, 269 (2002)
25. C.R. Lilley, M.N. Macrossan, *Phys. Fluids* **16**, 2054 (2004)
26. M.A. Gallis, R.B. Bond, J.R. Torczynski, *J. Chem. Phys.* **131**, 124311 (2009)
27. G.A. Lukyanov, Y. Khang, D.V. Leshchev, S.V. Kozyrev, A.N. Volkov, N.Y. Bykov, O.I. Vakulova, *Fuller. Nanotub. Carbon Nanostructures* **14**, 507 (2006)
28. N.Y. Bykov, G.A. Lukyanov, *Thermophys. Aeromech.* **13**, 523 (2006)
29. R. Jansen, I. Wysong, S. Gimelshein, M. Zeifman, U. Buck, *J. Chem. Phys.* **132**, 244105 (2010)
30. T.E. Itina, J. Hermann, P. Delaporte, M. Sentis, *Phys. Rev. E* **66**, 066406 (2002)
31. P. Politzer, P. Lane, M.E. Grice, *J. Phys. Chem. A* **105**, 7473 (2001)
32. C. Borgnakke, P.S. Larsen, *J. Comput. Phys.* **18**, 405 (1975)
33. C. Cercignani, *Rarefied Gas Dynamics: From Basic Concepts to Actual Calculations* (Cambridge University Press, Cambridge, 2000)
34. R.E. Honig, D.A. Kramer, *RCA Rev.* **30**, 285 (1969)
35. J.C. Maxwell, *Philos. Trans. R. Soc. Lond.* **170**, 231 (1879)
36. W.R. Harp, J.R. Dilwith, J.F. Tu, *J. Mater. Process. Technol.* **198**, 22 (2008)
37. A.R. Karagozian, *Prog. Energy Combust. Sci.* **36**, 531 (2010)